Research Article | Vol. 31, No. 13 / 19 Jun 2023 / Optics Express 20750
Optics EXPRESS

Enhanced efficiency of launching hyperbolic phonon polaritons in stacked α-MoO_3 flakes

KUN WANG,[1] HUA LONG,[1,4] NAN DENG,[1] MENG YUAN,[1] BING WANG,[1] KAI WANG,[1,2,*] AND PEIXIANG LU[1,3]

[1] *Wuhan National Laboratory for Optoelectronics and School of Physics, Huazhong University of Science and Technology, Wuhan 430074, China*
[2] *School of Electronic and Information Engineering, Hubei University of Science and Technology, Xianning 437100, China*
[3] *Hubei Key Laboratory of Optical information and Pattern Recognition, Wuhan Institute of Technology, Wuhan 430205, China*
[4] *longhua@hust.edu.cn*
[*] *kale_wong@hust.edu.cn*

Abstract: In this work, we reported a systemic study on the enhanced efficiency of launching hyperbolic phonon polaritons (PhPs) in stacked α-phase molybdenum trioxide (α-MoO_3) flakes. By using the infrared photo-induced force microscopy (PiFM), real-space near-field images (PiFM images) of mechanically exfoliated α-MoO_3 thin flakes were recorded within three different Reststrahlen bands (RBs). As referred with PiFM fringes of the single flake, PiFM fringes of the stacked α-MoO_3 sample within the RB 2 and RB 3 are greatly improved with the enhancement factor (EF) up to 170%. By performing numerical simulations, it reveals that the general improvement in near-field PiFM fringes arises from the existence of a nanoscale thin dielectric spacer in the middle part between two stacked α-MoO_3 flakes. The nanogap acts as a nanoresonator for prompting the near-field coupling of hyperbolic PhPs supported by each flake in the stacked sample, contributing to the increase of polaritonic fields, and verifying the experimental observations Our findings could offer fundamental physical investigations into the effective excitation of PhPs and will be helpful for developing functional nanophotonic devices and circuits.

1. Introduction

Van der Waals (vdW) materials are layered systems where atomic thin two-dimensional (2D) crystalline planes are bonded by the weak vdW force [1,2]. These vdW materials exhibit extreme anisotropic optical properties, and host a full site of polaritonic modes with a high degree of the electromagnetic wave confinement, covering from the ultraviolet to microwave spectrum [3–5]. In the past decades, phonon polaritons (PhPs) has been explored in vdW crystals including the hexagonal boron nitride (h-BN) [6], α-phase molybdenum trioxide (α-MoO_3) [7–9] and metal oxide α-V_2O_5 [10] crystal flake. The PhPs are collective modes that involves the coupling of photons with infrared active phonons [11]. Due to the weak phonon damping and extreme optical confinement, PhPs in vdW materials promise the potential for a various of technologically important applications in the IR spectrum, such as subdiffractional imaging [12], thermal energy steering [13], and ultrasensitive molecular sensing [14,15]. Efficiently launching and tuning of PhPs at the subwavelength scale are important for the development of infrared on-chip nanodevices. Since the large momenta of PhPs, it is not possible to directly excite PhPs on flat vdW flakes without any nanostructures by the incident light in free space [16]. For compensating the momentum mismatch and effectively launching PhPs, a series of methods that include the sharp tip of the near-field microscopy [17], metallic edges [18], resonant plasmonic rod antennas [19], a single silver nanoantenna [20], and discontinuities locations

#493972 https://doi.org/10.1364/OE.493972
Journal © 2023 Received 26 Apr 2023; revised 21 May 2023; accepted 25 May 2023; published 5 Jun 2023

Optics EXPRESS

of vdW crystals, such as sample edges [21], surface impurities [22] and natural wrinkles [23] have been successfully demonstrated in experiment. Moreover, PhPs can be excited based on nanostructured vdW materials (e.g., cones, disks, rods and strips) [24,25].

Notably, by restacking various vdW materials to assemble vdW heterostructures, different polaritons can evanescently couple with each other [26], enabling unprecedented control of polaritonic response even at the single atomic plane level [27–29] and holding a promising strategy for launching PhPs. Two powerful approaches have been experimentally realized to manipulate PhPs at the subwavelength scale. One method is through the formation of moiré superlattices [30,31]. As a result of the twist-angle-dependent interlayer hybridization, photonic crystals for plasmon polaritons in moiré graphene superlattices have been studied [32]. The other one is based on the combination of strongly coupled polaritons and extreme anisotropy of ultra-low-loss PhPs in α-MoO_3, a representative biaxial vdW crystal [33,34]. Through the interlayer coupling of hyperbolic PhPs in stacked bilayers/trilayers α-MoO_3 flakes, moldable topological transitions of hyperbolic PhPs can be achieved over a broadband spectrum [35,36]. Besides the remarkable progress that has been made in manipulating of PhPs in stacked α-MoO_3 flakes through strongly coupled PhPs [37–39], it has not been explored in detail that its impact in the efficiency of launching PhPs in stacked α-MoO_3 flakes [28]. The clarity on the above effect could provide the insight on the excitation efficiency of PhPs in stacked α-MoO_3 flakes, with prospective outcomes for PhPs based flatland nanophotonic circuits, optical sensing, and novel quantum phenomena [40].

In this work, we investigated the polaritonic features of strongly coupled hyperbolic PhPs in the stacked α-MoO_3 flakes in real-space by utilizing the PiFM equipment. PiFM images of both the single and stacked flakes were obtained near the sample edges within three various RBs of the α-MoO_3 crystal. It was experimentally demonstrated that the stacked sample showed notable improvement for PiFM fringes with the enhancement factor (EF) up to 170% at the RB 2 and RB 3. To reveal the mechanism for the enhanced efficiency of launching PhPs in the stacked sample, we carried out numerical simulations with a structural model that a nanoscale air gap was inserted in the middle part of the stacked α-MoO_3 flakes under the consideration for the fabrication procedure of the stacked sample at ambient condition. Acting as a nanoresonator, the air gap could prominently strengthen the near-field coupling of hyperbolic PhPs supported by each α-MoO_3 flake. Hence, there is an increase in polaritonic field strength around the air gap area, indicating the enhanced excitation efficiency of hyperbolic PhPs in the stacked α-MoO_3 flakes. Our work can not only deepen the insight into the essential properties of hyperbolic PhPs in α-MoO_3 flakes, but also contribute towards the progress in bio-sensing, nanoimaging, and near-field heat energy management [41].

2. Experiment methods

Thin α-MoO_3 flakes were obtained by mechanically exfoliating an α-MoO_3 bulk crystal. The flakes were inspected through the commercial optical microscopy (BX 53, Olympus). Then we used a home-built micromechanical setup to transfer one selected flake on top of the bottom flake with alignment of their x crystalline orientation, i.e. the relative twisted angle between each flake in the stacked sample is near zero. All samples were fabricated on silicon substrates covered with 300 nm SiO_2 layers. The surface morphology of the α-MoO_3 flakes was detected by atomic force microscopy (AFM), see Fig.1a and 1b. A global Cartesian coordinate was used to describe the directions of the nanoscale thin flakes, where the crystalline directions of α-MoO_3 were defined as the x ([100]) and y ([001]) axes. Their height profiles were extracted from the atomic force microscopy images and marked by red dashed lines (see Fig. 1(a) and 1(b)). The thickness of the single α-MoO_3 flake in Fig. 1(a) is 300 nm, which is almost the same as the sum height of the stacked α-MoO_3 flakes in Fig. 1(b) (the thickness of the bottom and top flake are 165 nm and 135 nm, respectively).

Optics EXPRESS

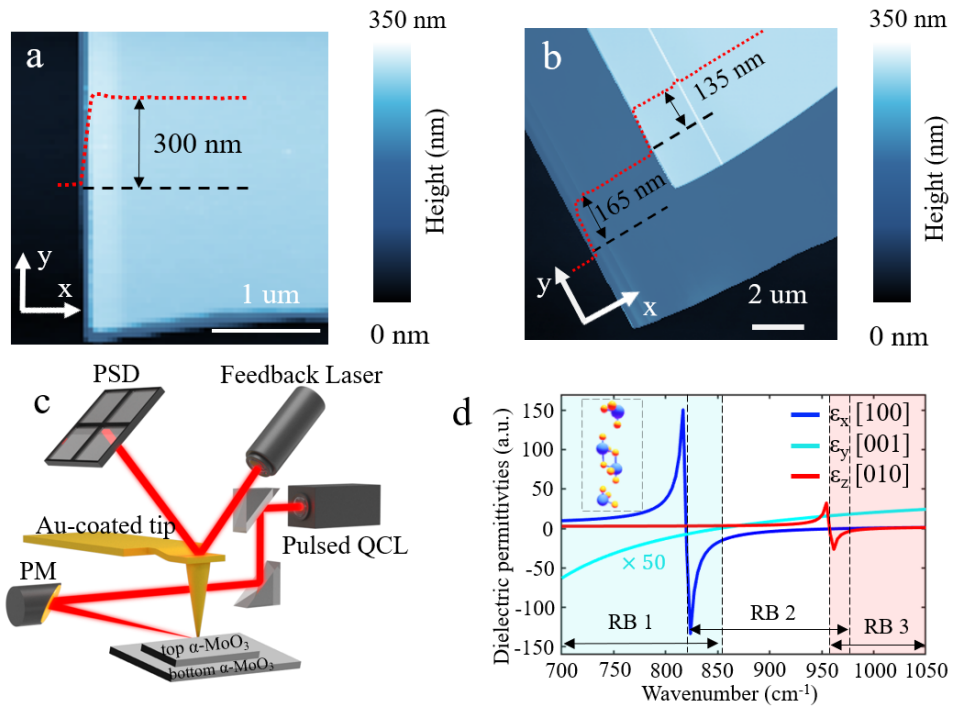

Fig. 1. The basic property of the α-MoO_3 crystal. Atomic force microscopy (AFM) images for (a) the single, and (b) stacked α-MoO_3 flakes. Red dotted lines are the extracted height profiles data for the corresponding flakes. Labels with arrows indicate crystalline directions of α-MoO_3. (c) Experimental schematic for photo-induced force microscopy (PiFM). PM: parabolic mirror, QCL: quantum cascade laser, PSD: position-sensitive detector. (d) The real part of the permittivity tensors of the α-MoO_3 crystal along its three principle axes. Inset: the unit cell of the α-MoO_3 crystal (top left).

In order to experimentally nanoimaging the hyperbolic PhPs of α-MoO_3 flakes, we employed the infrared near-field technique based on photo-induced force microscopy (Fig. 1(c), Molecular Vista). The oscillating Au-coated AFM tip is illuminated with p-polarized pulsed laser (QCL, Block Engineering) and the laser wavenumber can be tuned between 765 and 1700cm^{-1}. Acting as an infrared antenna, the metallic tip concentrates the incident infrared laser at its apex for exciting PhPs [42]. With the QCL modulated at the frequency difference between the first and second eigenmodes of the cantilever, the mechanical force detection channel (the PiFM signal, the first eigenmode of the cantilever) for PhPs is simultaneously recorded with the corresponding morphology (the second eigenmode of the cantilever) of the sample by two different eigenmodes of the AFM tip, yielding both the morphology and PiFM images with the nanoscale resolution [43,44].

Since the infrared spectral response of the α-MoO_3 crystal is dominated by the phonon absorption, the dielectric tensor along different crystalline directions of the α-MoO_3 crystal can be calculated by the multiple Lorentz oscillator model [9,11]. In Fig. 1(d), we plotted the real part of the permittivity tensors (Re(ε)) of the biaxial α-MoO_3 crystal along its three different principle axes. The spectrum ranges from 700 to 1050 cm^{-1}, which covers three different RBs of the α-MoO_3 crystal. The orthorhombic crystal structure of the α-MoO_3 crystal is shown in the inset of Fig. 1(d). This low symmetric crystalline structure of the α-MoO_3 crystal gives rise to rich phonon modes, which are infrared-active along three principle crystalline directions and thus yields various RBs [11]. In each RB that spans from the longitudinal optical (LO) over the

Optics EXPRESS

transverse optical (TO) phonon frequency of the α-MoO_3 crystal, the Re(ε) is expected to be negative and hyperbolic PhPs modes are supported by the α-MoO_3 crystal [45,46]. In Fig. 1(d), there are three RBs in the mid-infrared range of 700 to 1050 cm^{-1}. Specifically, the RB 1 covers from 700 to 851 cm^{-1}, the RB 2 ranges from 820 to 972 cm^{-1}, and the RB 3 spans from 958 over 1000 cm^{-1}, originating from the phonon modes along the x, y and z crystal directions of the α-MoO_3 crystal, respectively.

3. Results and discussion

To elucidate the enhancement of PiFM fringes of the stacked sample, we firstly investigated hyperbolic PhPs of the RB 2. Figure 2(a) and 2(b) show the PiFM images of the single flake recorded with the incident laser at 910 and 900 cm^{-1}, respectively. By utilizing the polariton interferometry nanoimaging method [42,47–49], the AFM tip excited hyperbolic PhPs in the α-MoO_3 flake. Then, tip-launched PhPs propagated outwards the x direction with a hyperbolic wavefront and were back-reflected while reaching the flake edge, giving rise to interference PiFM fringes with a spacing $\lambda_p/2$ (λ_p is the wavelength of hyperbolic PhPs). Notably, only PiFM fringes along with the y axis were observed since the propagation of PhPs within the RB 2 was forbidden along the y direction [7], and the absence of PhPs propagation in the y direction is consistent with in-plane hyperbolic PhPs dispersion [48]. These patterns of PiFM images are consistence with the previous study on in-plane hyperbolic PhPs of the α-MoO_3 flake within the RB 2 [7,8,47], thus validating the reliability of the PiFM technique. To make a direct comparison of these collected PiFM images between the single and stacked flakes, PiFM images of stacked α-MoO_3 flakes are collected at 910 (Fig. 1(c)) and 900 cm^{-1} (Fig. 1(d)). Besides a similar PiFM pattern shown in stacked flakes, they display highly improved patterns of PiFM fringes. In Addition, there was negligible interference PiFM fringes around the bottom flake of the stacked sample since the tip-launched hyperbolic PhPs at the bottom flake were rarely reflected back by the edge of the top α-MoO_3 flake in the stacked sample.

For clearly showing the contrast difference in PiFM fringes for both samples, we analyzed their respective line profiles of their PiFM images. These black and red dashed lines represent the PiFM data extracted from the single and stacked flakes, respectively. Those dashed lines are parallel to the crystal directions of the α-MoO_3 flake, as referred with the labelled arrows in PiFM images. As shown in Fig. 2(e), the PiFM signals profiles along x axis exhibits a series of oscillation maximum, induced by hyperbolic PhPs interferences. With the incident laser wavenumber (ω) fixed, the distance separation between the adjacent fringes of PiFM profiles of two above samples are very similar to each other. Since the separation distance of PiFM fringes could be used for calculating the wavelength (λ_p) of PhPs and the real part of the corresponding wavenumber (Re(q) = $2\pi/\lambda_p$), it implies that the wavenumber of PhPs is similar for both samples within the RB 2. Furthermore, it is obvious that the dashed lines (PiFM signals of the stacked flakes) exhibit a higher signal contrast than that of the solid lines (PiFM signals of the single flake). For quantitatively evaluating the contrast of the PiFM fringes, we defined the following equation:

$$C = \frac{PiFM_{peak} - PiFM_{valley}}{PiFM_{bulk}}, \tag{1}$$

where $PiFM_{peak}$ and $PiFM_{valley}$ are the first peak (maximum) and second valley (minimum) fringes of the PiFM signals, respectively. $PiFM_{bulk}$ means PiFM signals of α-MoO_3 flakes without PhPs existing, such as the area far away from the sample boundary, and the inner part of the α-MoO_3 flake. With ω = 900 cm^{-1}, the C for the single and stacked flakes is around 0.150 and 0.253, respectively. For ω = 910 cm^{-1}, the C for the single and stacked flakes is around 0.134 and 0.160, respectively. The enhancement factor (EF) of the PiFM signal is defined as the ratio between the C of the stacked sample to that of the single flake. The EF for PiFM collected ω at 900 and 910 cm^{-1} is 168% and 118%, respectively. Therefore, the PiFM fringes

Optics EXPRESS

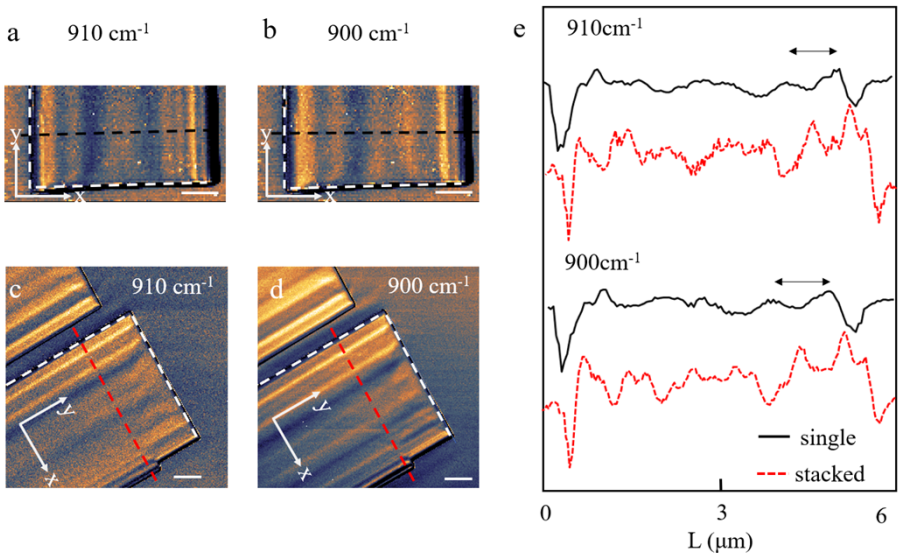

Fig. 2. Real-space nanoimaging of in-plane hyperbolic phonon polaritons on α-MoO_3 at the RB 2. PiFM images of the single α-MoO_3 flake taken with ω at (a) 910 and (b) 900 cm^{-1}. (c) and (d) are the near-field images of stacked α-MoO_3 flakes collected at ω = 910 and 900 cm^{-1}, respectively. Labelled arrows mean crystalline directions of α-MoO_3. Scale bars are 1 μm. (e) PiFM line profiles extracted from (a) to (d) with the black solid lines and red dashed lines denoted for the PiFM data collected from single and stacked α-MoO_3 flakes, respectively. Those line profiles of PiFM are aligned with the white dashed lines that represent the crystal directions of the α-MoO_3 flake.

are greatly improved for the stacked sample, suggesting an enhanced efficiency of launching in-plane hyperbolic PhPs at the RB 2.

Within the RB 3 of the α-MoO_3 crystal, the planar wavefront of PhPs is elliptical, and the wavelength of the elliptical PhPs along the y direction is longer than that along the x direction [7,9]. For the single α-MoO_3 flake, the PiFM fringes along both x and y directions can be observed but not distinct, as shown in Fig. 3(a) and 3(b). As for the stacked sample (Fig. 3(c) and 3(d)), the PiFM fringes of PhPs along both crystal directions are very obvious, and the separation distance of PiFM fringes along the y direction is longer than that along the x direction, confirming the in-plane elliptical wavefront of PhPs within the RB 3. For an evident comparison between the PiFM fringes of two samples within the RB 3, line profiles of four PiFM images along the x and y directions were plotted in Fig. 3(e) and 3(f), respectively. The solid black and dashed red lines are corresponding to the PiFM data drawn from the single and stacked samples, respectively. As compared with the solid black lines, these dashed lines show a pretty smooth line shape and enhanced PiFM fringes, meaning the increased excitation efficiency of PhPs for the stacked sample within the RB 3. The EF for ω at 985 cm^{-1} is 159% along x and 150% along y directions, respectively. Additionally, the EF is 161% in x and 169% in y directions at ω = 995 cm^{-1}. From the above experimental results of the single and stacked α-MoO_3 flakes within two RBs, there is an evident indication that the excitation efficiency of PhPs in stacked α-MoO_3 flakes is enhanced.

To unveil the improved near-field PiFM fringes of the stacked α-MoO_3 flakes within the above two RBs, we carried out full-wave numerical simulations by finite element method (FEM). Acting as an excitation source like the metallic AFM tip, a z-polarized electric dipole was placed along the z direction at 200 nm above the surface of the top α-MoO_3 flake. As a benchmark, we firstly simulated the case for a single α-MoO_3 flake with a thickness of 300 nm at ω = 900 cm^{-1} (the

Optics EXPRESS

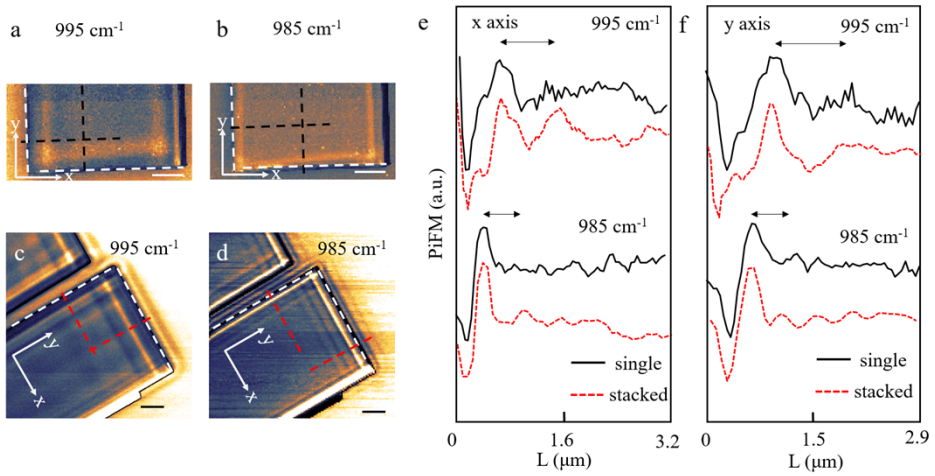

Fig. 3. Nanoimaging of out-of-plane hyperbolic phonon polaritons on α-MoO_3 at the RB 3 in real-space. PiFM images of the single α-MoO_3 flake taken with ω at (a) 995 and (b) 985 cm^{-1}. (c) and (d) are the near-field images of the stacked α-MoO_3 flakes collected at ω = 995 and 985 cm^{-1}, respectively. Labelled arrows represent crystal directions of the α-MoO_3 crystals. Scale bars are 1 μm. (e) and (f) are PiFM line profiles extracted along x and y directions, respectively. Black solid lines and red dashed lines denoted for the PiFM data collected from the single and stacked α-MoO_3 flakes, respectively. Those line profiles of PiFM are aligned with the white dashed lines that represent the crystal directions of the α-MoO_3 flake.

RB 2). The real part of the z-component of the electric field (Re(E_z)) was extracted from the cross-sectional (x–z plane including the dipole, XoZ) plane, as shown in Fig. 4(a). In Fig. 4(a), it is observed that the polaritonic field distribution of hyperbolic PhPs are mostly confined at the outside of the α-MoO_3 flake and the Re(E_z) gradually decay into the dielectric environment (the substrate and the air region). In Fig. 4(b), the distribution of Re(E_z) was extracted from the XoZ plane of the stacked flakes with ω at 900 cm^{-1}. Since stacked α-MoO_3 flakes was prepared under ambient condition, nanoscale dielectric gaps would be accidently introduced between two stacked flakes. For the modified numerical structure model, a 10 nm air gap was inserted in the middle part of the stacked sample. In comparison with the numerical results of the single flake (Fig. 4(a)), hyperbolic PhPs in the stacked sample (Fig. 4(b)) not only clearly show the elongated the polaritonic wavelength but also a polaritonic field distribution with a modestly increased dense confinement around the top surface of the stacked sample (Fig. 4(b)). As plotted in the inset of Fig. 4(b), the presence of air gap strongly enhances the vertical confinement and coupling of the polaritonic fields within the nanoscale gap area. In addition, the EF of at the center air gap region is around 5. Thus, the numerical results reveal that the excitation efficiency of hyperbolic PhPs within the RB 2 of the stacked sample is significantly increased.

As for hyperbolic PhPs of the RB 3 (ω = 980 cm^{-1}), the Re(E_z) of the XoZ plane of the single flake is shown in Fig. 4(c) and the polaritonic fields are mostly confined at the inside part of the flake (Fig. 4(c)). As for the Re(E_z) of the stacked sample (Fig. 4(d)), the wavelength of hyperbolic PhPs slightly shortens. The distribution of the Re(E_z) inside the gap region is plotted the inset of Fig. 4(d) with its EF at the central part of the air gap region is around 1.5. A previous study has been demonstrated that it is feasible to continually tune wavelength and lower damping rate of the hyperbolic PhPs by varying air gaps in a suspended α-MoO_3 flake over dielectric substrate (SiO_2) [50,51], which are consistent with the simulation results for the stacked sample. Moreover, the numerical simulation clarifies that although the air gap layer is only 10 nm in

Optics EXPRESS

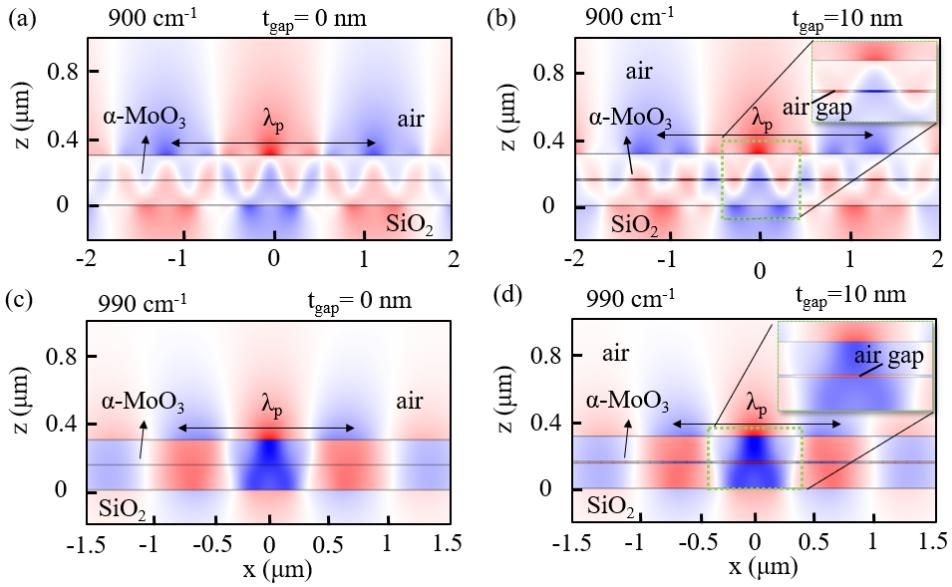

Fig. 4. The numerical simulation results for the single and stacked α-MoO_3 flakes. With $\omega = 900\,cm^{-1}$ (the RB 2), (a), and (b) are the simulated z-component for the electric field (Re(E_z) of the cross-sectional (XoZ) plane of structural models for the single and stacked samples. (b) Within the RB 3 ($\omega = 990\,cm^{-1}$), (c), and (d) are the simulated Re(E_z) of the XoZ plane of structural models for the single and stacked flakes. The insets (top right side) in (b) and (d) zoom into the distribution of the Re(E_z) at the 10 nm air gap region within two RBs, clearly demonstrating dramatic polaritonic field enhancement.

this stacked structural model, it can play a significant role in engineering the environment of hyperbolic PhPs within the RB 2 and RB 3. Besides the nanoscale air gap spacer, it is foreseen that another dielectric spacer with higher stability and reproducibility fabricated by the modern CMOS technique could be inserted in a polaritonic multilayer structure [52,53]. As a result of the good controllability of the dielectric spacer, it would be beneficial for high-performance integrated optical devices in dynamic control of chemical reactions, promoting interactions between polaritons with adjacent molecules, and heat energy transferring at the subwavelength scale [54].

Additionally, PiFM images of both samples were collected at the RB 1. As shown in Fig. 5(a) and 5(b), the single flake shows interference PiFM fringes with a low contrast. For the stacked sample, there is a distinct improvement in the PiFM fringes (Fig. 4(c) and 4(d)). Line profiles of PiFM images along the y direction are shown in Fig. 5(e). The EFs for PiFM fringes collected ω at 765 and 775 cm^{-1} are 104% and 129%, respectively. The EFs for PiFM fringes recorded at the RB 1 are largely reduced when compared with that measured at the RB 2 and RB 3. This could be explained by the periodicity of PiFM fringes in Fig. 5(a) - d. Specifically, the periodicity of PiFM fringes in the stacked sample corresponds to the polariton wavelength (λ_p), shown as red dashed lines in Fig. 5(e). Since the incident laser was guided perpendicular to the y axis of α-MoO_3 flakes, there was a projection of E-field of the pulsed p-polarized QCL along the same direction and hyperbolic PhPs could be directly launched by the sample edge, which propagated as a plane wave with a fringe periodicity of λ_p [21,22]. However, for the case of the single flake, the polariton was dominantly excited by the tip with interference fringes of $\lambda_p/2$ (black solid lines in Fig. 5(e)). It has been reported that the tip-launched polaritons propagate as circular waves and the amplitude of a circular wave decreases, whereas that of the plane wave does not [22].

Optics EXPRESS

Therefore, the C of the stacked sample becomes smaller than that of the single flake, leading to a decrease in the corresponding EFs of PiFM fringes within the RB 1.

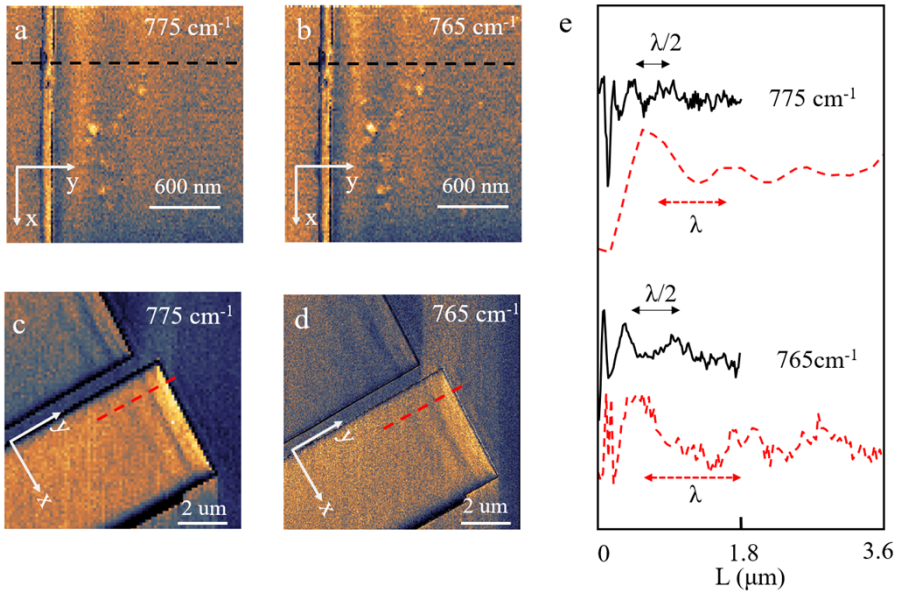

Fig. 5. Real-space imaging of in-plane hyperbolic phonon polaritons on α-MoO_3 at the RB 1. PiFM images of the single α-MoO_3 flake taken with ω at (a) 775, and (b) 765 cm^{-1}. (c), and (d) are the near-field images of stacked α-MoO_3 flakes collected with at ω = 775, and 765 cm^{-1}, respectively. Labelled arrows indicate crystal directions. (e) PiFM line profiles extracted from (a) to (d) with the black solid lines, and red dashed lines denoted for the PiFM data collected from the single and stacked α-MoO_3 flakes, respectively. The fringe periodicity for black solid lines and red dashed lines are λ_p and $\lambda_p/2$, respectively. Those line profiles of PiFM are aligned with the y crystal direction of the α-MoO_3 flake.

Previously, it was shown that the excitation efficiency of PhPs in a single hBN flake by the AFM tip was superior to that of the sample edge [22], which is stark contrast to the above experimental observations of hyperbolic PhPs in the stacked α-MoO_3 sample within the RB 1. According to the above PiFM data of hyperbolic PhPs in the stacked α-MoO_3 flakes, the edge of the top flake in the stacked sample launched hyperbolic PhPs at the RB 1 more effectively than that of the AFM tip. The enhanced efficiency of edge-launched hyperbolic PhPs in the stacked α-MoO_3 flakes could be attributed to a combined effect that includes the nanoscale air gap between stacked sample and the wavenumber direction of the incident laser perpendicular to the sample edge. Notably, it is still a challenge to perform monochromatic scattering-type scanning near-field optical microscopy (s-SNOM) to probe hyperbolic PhPh at the RB 1 owing to the external interferometric detection method and the limitation of the available light sources [9,45]. Besides s-SNOM, PiFM could be an alternative optical near-field experimental instrument, especially for ω below 880 cm^{-1} [42,55].

4. Conclusion

In summary, we presented that the PiFM fringes of strongly coupled hyperbolic PhPs in stacked α-MoO_3 flakes were significantly enhanced in comparison with that for a single flake of a similar thickness. The infrared nanoimaging technique (PiFM) was performed to demonstrate that the enhancement factors of PiFM fringes for hyperbolic PhPs in the RB 2 and RB 3 were up to 170%. In the numerical simulation structural model, a nanoscale thin air gap is placed at the

Optics EXPRESS

central part of the stacked flakes. The simulated results suggest that the 10 nm air gap could be treated as a nanoresonator that enables the prominent near-field coupling of hyperbolic PhPs supported by each α-MoO_3 flake. Our study deepens the fundamental understanding of the near-field enhancement of coupled PhPs in the stacked double-layer polaritonic system and may promote advances in mid-infrared nanophotonics with efficient performance [56,57].

Funding. National Key Research and Development Program of China (2022YFA1604403); National Natural Science Foundation of China (11904271, 12021004, 12274157, 12274334); Basic and Applied Basic Research Foundation of Guangdong Province (2019B030302003).

Disclosures. The authors declare no conflicts of interest.

Data availability. Data underlying the results presented in this paper are not publicly available at this time but may be obtained from the authors upon reasonable request.

References

1. D. N. Basov, M. M. Fogler, and F. J. G. de Abajo, "Polaritons in van der Waals materials," Science 354(6309), (2016).
2. F. Xia, H. Wang, D. Xiao, M. Dubey, and A. Ramasubramaniam, "Two-dimensional material nanophotonics," Nat. Photonics **8**(12), 899–907 (2014).
3. A. Rodin, M. Trushin, A. Carvalho, and A. H. Castro Neto, "Collective excitations in 2D materials," Nat. Rev. Phys. **2**(10), 524–537 (2020).
4. T. Sang, Y. Pei, Q. Mi, S. Li, C. Yang, Y. Wang, and G. Cao, "Lithography-free tunable absorber at visible region via one-dimensional photonic crystals consisting of an α-MoO_3 layer," Opt. Express **30**(9), 14408–14420 (2022).
5. C. Wei, S. Abedini Dereshgi, X. Song, A. Murthy, V. P. Dravid, T. Cao, and K. Aydin, "Polarization Reflector/Color Filter at Visible Frequencies via Anisotropic α-MoO_3," Adv. Opt. Mater. **8**(11), 2000088 (2020).
6. S. Dai, Z. Fei, Q. Ma, A. S. Rodin, M. Wagner, A. S. McLeod, M. K. Liu, W. Gannett, W. Regan, K. Watanabe, T. Taniguchi, M. Thiemens, G. Dominguez, A. H. Castro Neto, A. Zettl, F. Keilmann, P. Jarillo-Herrero, M. M. Fogler, and D. N. Basov, "Tunable phonon polaritons in atomically thin van der Waals crystals of boron nitride," Science **343**(6175), 1125–1129 (2014).
7. W. Ma, P. Alonso-Gonzalez, S. Li, A. Y. Nikitin, J. Yuan, J. Martin-Sanchez, J. Taboada-Gutierrez, I. Amenabar, P. Li, S. Velez, C. Tollan, Z. Dai, Y. Zhang, S. Sriram, K. Kalantar-Zadeh, S. T. Lee, R. Hillenbrand, and Q. Bao, "In-plane anisotropic and ultra-low-loss polaritons in a natural van der Waals crystal," Nature **562**(7728), 557–562 (2018).
8. Z. Zheng, J. Chen, Y. Wang, X. Wang, X. Chen, P. Liu, J. Xu, W. Xie, H. Chen, S. Deng, and N. Xu, "Highly Confined and Tunable Hyperbolic Phonon Polaritons in Van Der Waals Semiconducting Transition Metal Oxides," Adv. Mater. **30**(13), 1705318 (2018).
9. Z. Zheng, N. Xu, S. L. Oscurato, M. Tamagnone, F. Sun, Y. Jiang, Y. Ke, J. Chen, W. Huang, W. L. Wilson, A. Ambrosio, S. Deng, and H. Chen, "A mid-infrared biaxial hyperbolic van der Waals crystal," Sci. Adv. **5**(5), eaav8690 (2019).
10. J. Taboada-Gutierrez, G. Alvarez-Perez, and J. Duan, *et al.*, "Broad spectral tuning of ultra-low-loss polaritons in a van der Waals crystal by intercalation," Nat. Mater. **19**(9), 964–968 (2020).
11. G. Hu, J. Shen, C. W. Qiu, A. Alù, and S. Dai, "Phonon Polaritons and Hyperbolic Response in van der Waals Materials," Adv. Opt. Mater. **8**(5), 1901393 (2020).
12. P. Li, M. Lewin, A. V. Kretinin, J. D. Caldwell, K. S. Novoselov, T. Taniguchi, K. Watanabe, F. Gaussmann, and T. Taubner, "Hyperbolic phonon-polaritons in boron nitride for near-field optical imaging and focusing," Nat. Commun. **6**(1), 7507 (2015).
13. S. Kim, S. G. Menabde, V. W. Brar, and M. S. Jang, "Functional Mid-Infrared Polaritonics in van der Waals Crystals," Adv. Opt. Mater. **8**(5), 1901194 (2020).
14. M. Autore, P. Li, I. Dolado, F. J. Alfaro-Mozaz, R. Esteban, A. Atxabal, F. Casanova, L. E. Hueso, P. Alonso-Gonzalez, J. Aizpurua, A. Y. Nikitin, S. Velez, and R. Hillenbrand, "Boron nitride nanoresonators for phonon-enhanced molecular vibrational spectroscopy at the strong coupling limit," Light: Sci. Appl. **7**(4), 17172 (2017).
15. A. Bylinkin, M. Schnell, M. Autore, F. Calavalle, P. Li, J. Taboada-Gutièrrez, S. Liu, J. H. Edgar, F. Casanova, L. E. Hueso, P. Alonso-Gonzalez, A. Y. Nikitin, and R. Hillenbrand, "Real-space observation of vibrational strong coupling between propagating phonon polaritons and organic molecules," Nat. Photonics **15**(3), 197–202 (2021).
16. Q. Zhang, G. Hu, W. Ma, P. Li, A. Krasnok, R. Hillenbrand, A. Alu, and C. W. Qiu, "Interface nano-optics with van der Waals polaritons," Nature **597**(7875), 187–195 (2021).
17. S. G. Menabde, S. Boroviks, J. Ahn, J. T. Heiden, K. Watanabe, T. Taniguchi, T. Low, D. K. Hwang, N. A. Mortensen, and M. S. Jang, "Near-field probing of image phonon-polaritons in hexagonal boron nitride on gold crystals," Sci. Adv. **8**(28), eabn0627 (2022).
18. A. J. Sternbach, S. H. Chae, S. Latini, A. A. Rikhter, Y. Shao, B. Li, D. Rhodes, B. Kim, P. J. Schuck, X. Xu, X. Y. Zhu, R. D. Averitt, J. Hone, M. M. Fogler, A. Rubio, and D. N. Basov, "Programmable hyperbolic polaritons in van der Waals semiconductors," Science **371**(6529), 617–620 (2021).

Optics EXPRESS

19. P. Alonso-Gonzalez, A. Y. Nikitin, F. Golmar, A. Centeno, A. Pesquera, S. Velez, J. Chen, G. Navickaite, F. Koppens, A. Zurutuza, F. Casanova, L. E. Hueso, and R. Hillenbrand, "Controlling graphene plasmons with resonant metal antennas and spatial conductivity patterns," Science **344**(6190), 1369–1373 (2014).
20. Z. Zheng, F. Sun, W. Huang, J. Jiang, R. Zhan, Y. Ke, H. Chen, and S. Deng, "Phonon Polaritons in Twisted Double-Layers of Hyperbolic van der Waals Crystals," Nano Lett. **20**(7), 5301–5308 (2020).
21. F. Hu, Y. Luan, M. E. Scott, J. Yan, D. G. Mandrus, X. Xu, and Z. Fei, "Imaging exciton–polariton transport in $MoSe_2$ waveguides," Nat. Photonics **11**(6), 356–360 (2017).
22. S. Dai, Q. Ma, Y. Yang, J. Rosenfeld, M. D. Goldflam, A. McLeod, Z. Sun, T. I. Andersen, Z. Fei, M. Liu, Y. Shao, K. Watanabe, T. Taniguchi, M. Thiemens, F. Keilmann, P. Jarillo-Herrero, M. M. Fogler, and D. N. Basov, "Efficiency of Launching Highly Confined Polaritons by Infrared Light Incident on a Hyperbolic Material," Nano Lett. **17**(9), 5285–5290 (2017).
23. L. Gilburd, K. S. Kim, K. Ho, D. Trajanoski, A. Maiti, D. Halverson, S. de Beer, and G. C. Walker, "Hexagonal Boron Nitride Self-Launches Hyperbolic Phonon Polaritons," J. Phys. Chem. Lett. **8**(10), 2158–2162 (2017).
24. W. Huang, F. Sun, Z. Zheng, T. G. Folland, X. Chen, H. Liao, N. Xu, J. D. Caldwell, H. Chen, and S. Deng, "Van der Waals Phonon Polariton Microstructures for Configurable Infrared Electromagnetic Field Localizations," Adv. Sci. **8**, 2004872 (2021).
25. J. Duan, F. J. Alfaro-Mozaz, J. Taboada-Gutierrez, I. Dolado, G. Alvarez-Perez, E. Titova, A. Bylinkin, A. I. F. Tresguerres-Mata, J. Martin-Sanchez, S. Liu, J. H. Edgar, D. A. Bandurin, P. Jarillo-Herrero, R. Hillenbrand, A. Y. Nikitin, and P. Alonso-Gonzalez, "Active and Passive Tuning of Ultranarrow Resonances in Polaritonic Nanoantennas," Adv. Mater. **34**(10), e2104954 (2022).
26. M. Yankowitz, Q. Ma, P. Jarillo-Herrero, and B. J. LeRoy, "van der Waals heterostructures combining graphene and hexagonal boron nitride," Nat. Rev. Phys. **1**(2), 112–125 (2019).
27. S. Abedini Dereshgi, M. C. Larciprete, M. Centini, A. A. Murthy, K. Tang, J. Wu, V. P. Dravid, and K. Aydin, "Tuning of Optical Phonons in α-MoO_3-VO_2 Multilayers," ACS Appl. Mater. Interfaces **13**(41), 48981–48987 (2021).
28. A. Yadav, R. Kumari, S. K. Varshney, and B. Lahiri, "Tunable phonon-plasmon hybridization in α-MoO_3-graphene based van der Waals heterostructures," Opt. Express **29**(21), 33171–33183 (2021).
29. A. Fali, S. T. White, T. G. Folland, M. He, N. A. Aghamiri, S. Liu, J. H. Edgar, J. D. Caldwell, R. F. Haglund, and Y. Abate, "Refractive Index-Based Control of Hyperbolic Phonon-Polariton Propagation," Nano Lett. **19**(11), 7725–7734 (2019).
30. G. Abbas, Y. Li, H. Wang, W. X. Zhang, C. Wang, and H. Zhang, "Recent Advances in Twisted Structures of Flatland Materials and Crafting Moiré Superlattices," Adv. Funct. Mater. **30**(36), 2000878 (2020).
31. Y. Luo, R. Engelke, M. Mattheakis, M. Tamagnone, S. Carr, K. Watanabe, T. Taniguchi, E. Kaxiras, P. Kim, and W. L. Wilson, "In situ nanoscale imaging of moire superlattices in twisted van der Waals heterostructures," Nat. Commun. **11**(1), 4209 (2020).
32. S. S. Sunku, G. X. Ni, B. Y. Jiang, H. Yoo, A. Sternbach, A. S. McLeod, T. Stauber, L. Xiong, T. Taniguchi, K. Watanabe, P. Kim, M. M. Fogler, and D. N. Basov, "Photonic crystals for nano-light in moire graphene superlattices," Science **362**(6419), 1153–1156 (2018).
33. M. Chen, X. Lin, T. H. Dinh, Z. Zheng, J. Shen, Q. Ma, H. Chen, P. Jarillo-Herrero, and S. Dai, "Configurable phonon polaritons in twisted α-MoO_3," Nat. Mater. **19**(12), 1307–1311 (2020).
34. J. Duan, N. Capote-Robayna, J. Taboada-Gutierrez, G. Alvarez-Perez, I. Prieto, J. Martin-Sanchez, A. Y. Nikitin, and P. Alonso-Gonzalez, "Twisted Nano-Optics: Manipulating Light at the Nanoscale with Twisted Phonon Polaritonic Slabs," Nano Lett. **20**(7), 5323–5329 (2020).
35. C. Zheng, G. Hu, X. Liu, X. Kong, L. Wang, and C. W. Qiu, "Molding Broadband Dispersion in Twisted Trilayer Hyperbolic Polaritonic Surfaces," ACS Nano **16**(8), 13241–13250 (2022).
36. G. Hu, Q. Ou, G. Si, Y. Wu, J. Wu, Z. Dai, A. Krasnok, Y. Mazor, Q. Zhang, Q. Bao, C. W. Qiu, and A. Alu, "Topological polaritons and photonic magic angles in twisted α-MoO_3 bilayers," Nature **582**(7811), 209–213 (2020).
37. H. Hu, N. Chen, H. Teng, R. Yu, Y. Qu, J. Sun, M. Xue, D. Hu, B. Wu, C. Li, J. Chen, M. Liu, Z. Sun, Y. Liu, P. Li, S. Fan, F. J. Garcia de Abajo, and Q. Dai, "Doping-driven topological polaritons in graphene/α-MoO_3 heterostructures," Nat. Nanotechnol. **17**(9), 940–946 (2022).
38. F. L. Ruta, B. S. Y. Kim, Z. Sun, D. J. Rizzo, A. S. McLeod, A. Rajendran, S. Liu, A. J. Millis, J. C. Hone, and D. N. Basov, "Surface plasmons induce topological transition in graphene/α-MoO_3 heterostructures," Nat. Commun. **13**(1), 3719 (2022).
39. Y. Zeng, Q. Ou, L. Liu, C. Zheng, Z. Wang, Y. Gong, X. Liang, Y. Zhang, G. Hu, Z. Yang, C.-W. Qiu, Q. Bao, H. Chen, and Z. Dai, "Tailoring Topological Transitions of Anisotropic Polaritons by Interface Engineering in Biaxial Crystals," Nano Lett. **22**(10), 4260–4268 (2022).
40. D. N. Basov, A. Asenjo-Garcia, P. J. Schuck, X. Zhu, and A. Rubio, "Polariton panorama," Nanophotonics **10**(1), 549–577 (2020).
41. S. Foteinopoulou, G. C. R. Devarapu, G. S. Subramania, S. Krishna, and D. Wasserman, "Phonon-polaritonics: enabling powerful capabilities for infrared photonics," Nanophotonics **8**(12), 2129–2175 (2019).
42. A. Ambrosio, M. Tamagnone, K. Chaudhary, L. A. Jauregui, P. Kim, W. L. Wilson, and F. Capasso, "Selective excitation and imaging of ultraslow phonon polaritons in thin hexagonal boron nitride crystals," Light: Sci. Appl. **7**(1), 27 (2018).

Optics EXPRESS

43. J. Liu, S. Park, D. Nowak, M. Tian, Y. Wu, H. Long, K. Wang, B. Wang, and P. Lu, "Near-Field Characterization of Graphene Plasmons by Photo-Induced Force Microscopy," Laser Photonics Rev. **12**(8), 1800040 (2018).
44. M. Poblet, Y. Li, E. Cortes, S. A. Maier, G. Grinblat, and A. V. Bragas, "Direct Detection of Optical Forces of Magnetic Nature in Dielectric Nanoantennas," Nano Lett. **20**(10), 7627–7634 (2020).
45. W. Dong, R. Qi, T. Liu, Y. Li, N. Li, Z. Hua, Z. Gao, S. Zhang, K. Liu, J. Guo, and P. Gao, "Broad-Spectral-Range Sustainability and Controllable Excitation of Hyperbolic Phonon Polaritons in α-MoO_3," Adv. Mater. **32**(46), 2002014 (2020).
46. J. J. Schwartz, S. T. Le, S. Krylyuk, C. A. Richter, A. V. Davydov, and A. Centrone, "Substrate-mediated hyperbolic phonon polaritons in α-MoO_3," Nanophotonics **10**(5), 1517–1527 (2021).
47. J. Huang, L. Tao, N. Dong, H. Wang, S. Zhou, J. Wang, X. He, and K. Wu, "In-Plane Hyperbolic Phonon-Polaritons in van der Waals Nanocrystals," Adv. Opt. Mater. **11**(5), 2202048 (2023).
48. P. Li, I. Dolado, F. J. Alfaro-Mozaz, F. Casanova, L. E. Hueso, S. Liu, J. H. Edgar, A. Y. Nikitin, S. Velez, and R. Hillenbrand, "Infrared hyperbolic metasurface based on nanostructured van der Waals materials," Science **359**(6378), 892–896 (2018).
49. N. Deng, H. Long, K. Wang, X. Han, B. Wang, K. Wang, and P. Lu, "Giant optical anisotropy of WS_2 flakes in the visible region characterized by Au substrate assisted near-field optical microscopy," Nanotechnology **33**(34), 345201 (2022).
50. Z. Zheng, F. Sun, N. Xu, W. Huang, X. Chen, Y. Ke, R. Zhan, H. Chen, and S. Deng, "Tunable Hyperbolic Phonon Polaritons in a Suspended van der Waals α-MoO_3 with Gradient Gaps," Adv. Opt. Mater. **10**(5), 2102057 (2022).
51. J. Shen, Z. Zheng, T. Dinh, C. Wang, M. Chen, P. Chen, Q. Ma, P. Jarillo-Herrero, L. Kang, and S. Dai, "Hyperbolic phonon polaritons with positive and negative phase velocities in suspended α-MoO_3," Appl. Phys. Lett. **120**(11), 113101 (2022).
52. F. H. Feres, R. A. Mayer, I. D. Barcelos, R. O. Freitas, and F. C. B. Maia, "Acceleration of Subwavelength Polaritons by Engineering Dielectric-Metallic Substrates," ACS Photonics **7**(6), 1396–1402 (2020).
53. F. Lv, Z. Wang, Y. Huang, J. Chen, J. La, D. Wu, Z. Guo, Y. Liu, Y. Zhang, Y. Wang, and W. Wang, "Strong coupling between monolayer quantum emitter WS_2 and degenerate/non-degenerate surface lattice resonances," Opt. Lett. **47**(1), 190–193 (2022).
54. S. G. Menabde, J. T. Heiden, J. D. Cox, N. A. Mortensen, and M. S. Jang, "Image polaritons in van der Waals crystals," Nanophotonics **11**(11), 2433–2452 (2022).
55. Y. Zhao, J. Chen, M. Xue, R. Chen, S. Jia, J. Chen, L. Bao, H. J. Gao, and J. Chen, "Ultralow-Loss Phonon Polaritons in the Isotope-Enriched α-MoO_3," Nano Lett. **22**(24), 10208–10215 (2022).
56. Y. Wu, J. Duan, W. Ma, Q. Ou, P. Li, P. Alonso-González, J. D. Caldwell, and Q. Bao, "Manipulating polaritons at the extreme scale in van der Waals materials," Nat. Rev. Phys. **4**(9), 578–594 (2022).
57. M. He, T. G. Folland, J. Duan, P. Alonso-González, S. De Liberato, A. Paarmann, and J. D. Caldwell, "Anisotropy and Modal Hybridization in Infrared Nanophotonics Using Low-Symmetry Materials," ACS Photonics **9**(4), 1078–1095 (2022).